JCB Journal of Cell Biology

REPORT

Close-up of vesicular ER exit sites by volume electron imaging using FIB-SEM

Athul Nair[2], Akhil Nair[2], Patrick Stock[2], Arkash Jain[2], Elliott Somerville[2], Anwesha Sanyal[1,2], Jose Inacio Costa-Filho[1,2], and Tom Kirchhausen[1,2,3]

The architecture of ER exit sites (ERES), the first sites of membrane remodeling in protein secretion, remains unclear, with descriptions ranging from vesicular clusters to extended tubular structures. We addressed this divergence by visualizing ERES in cells not overexpressing secretory cargo using large-scale volume-focused ion beam scanning EM (FIB-SEM) after high-pressure freeze substitution. Automated segmentation in EM (ASEM), our 3D U-Net pipeline trained with sparsely labeled 50–70-nm COPI vesicles near the Golgi, accurately detected them in HeLa, SVG-A, and iPSC-derived neurons. Using the same model, we identified abundant clusters of ∼5–40 larger vesicles (∼65–85 nm) confined within ∼250 nm^3 regions adjacent to flattened ER domains, consistent with vesicular ERES. Similar assemblies also appeared alongside tubular networks and varicosities extending from enlarged ER domains, previously described as the sole ERES in HeLa cells. These findings reveal that vesicular ERES are widespread and morphologically diverse, resolving longstanding contradictions in early secretory pathway organization.

Introduction

Volume EM provides unparalleled snapshots views into the 3D subcellular organization, offering a wealth of contextual information critical for understanding membrane dynamics. Among these, focused ion beam scanning EM (FIB-SEM) enables large-scale, 3D imaging of intracellular structures with near-isotropic high resolution. Most FIB-SEM datasets achieve 8-nm resolution (Narayan et al., 2014; Knott et al., 2008; Xu et al., 2017; Wu et al., 2017; Hoffman et al., 2020), with recent developments reaching 4–5 nm (e.g., [Xu et al., 2021; Müller et al., 2020; Sanyal et al., 2024; Gallusser et al., 2022; Weigel et al., 2021; Heinrich et al., 2021]). When applied to cells preserved by high-pressure freezing and freeze substitution (HPFS), FIB-SEM maintains native ultrastructure while providing a comprehensive view of macromolecular assemblies, membranes, and organelles within individual cells or even across clusters of cells in intact tissues. This approach has detected spatial relationships that were previously obscured by the limited depth of field in conventional thin-section transmission EM (TEM), which images 30- to 300-nm-thick sections, representing only a small fraction of the whole cell (e.g., [Ladinsky et al., 1994; Zeuschner et al., 2006; Mironov et al., 2003]).

Despite its potential, the complexity of such FIB-SEM datasets makes direct visual inspection impractical. To address this limitation, AI-based methods powered by sparsely labeled ground truths and 3D U-Net convolutional neural networks have been developed to automate segmentation, greatly improving the identification and characterization of subcellular structures (Heinrich et al., 2021; Gallusser et al., 2022; Mekuč et al., 2022). The Cell organelle segmentation in EM (COSEM) project at the Janelia Research Campus uses deep learning to train models for detecting and quantifying intracellular structures within large-scale EM datasets (Xu et al., 2021). The automated segmentation of intracellular structures in EM (ASEM) pipeline, independently developed by our group, also uses deep neural networks to identify organelles ranging from clathrin-coated vesicles (CCVs) and nuclear pores to mitochondria, the Golgi apparatus, and the ER (Gallusser et al., 2022; Galbraith, 2023). These AI-driven approaches now greatly accelerate the detailed characterization of organelles in both normal (Gallusser et al., 2022; Heinrich et al., 2021) and metabolically altered states (Parlakgül et al., 2022).

Taking advantage of these advances, we investigated a fundamental membrane remodeling event concerning the anterograde trafficking of cargo from the ER to the Golgi apparatus. Trafficking that originates at ER exit sites (ERES) was initially proposed to involve COPII coat assembly at the ER surface, with the resulting ∼50–70-nm COPII-coated vesicles then functioning as transport carriers (Balch et al., 1994) (reviewed by Béthune

[1]Department of Cell Biology, Harvard Medical School, Boston, MA, USA; [2]Program in Cellular and Molecular Medicine, Boston Children's Hospital, Boston, MA, USA; [3]Department of Pediatrics, Harvard Medical School, Boston, MA, USA.

Correspondence to Tom Kirchhausen: kirchhausen@crystal.harvard.edu.

https://doi.org/10.1083/jcb.202504178

and Wieland [2018]). Support for this model originated from *in vitro* reconstitution assays showing formation of ∼50-nm COPII vesicles from ER membranes of yeast and mammalian cells (reviewed by Béthune and Wieland [2018]). High-resolution 3D immuno-gold labeling TEM of ∼400-nm sections of frozen human liver–derived HepG2 cells provided further *in vivo* morphological evidence, revealing COPII and cargo-containing 50–60-nm vesicles alongside ∼200-nm tubular structures near expanded ER domains (Zeuschner et al., 2006). Cryo-tomography of cryo-FIB milled INS-1 rat insulinoma cells active in secretion showing ω-shaped buds emerging from flattened ER cisternae, closely associated with clusters of ∼52–64-nm coated and uncoated vesicles, as well as small ∼100-nm pearled tubules, but the resolution was insufficient to definitively identify the vesicle coat type (Carter et al., 2020). Flattened ER refers to extended cisternal sheets with a reduced luminal width and low curvature, which serve as distinct domains contrasted with tubular or varicose ER in 3D reconstructions. The tubules might correspond to the previously proposed "mega-carriers" or extended tubular carriers implicated in the ER-to-Golgi transport of large cargoes, such as lipoproteins and ∼300-nm procollagen assemblies (Gorur et al., 2017; Raote and Malhotra, 2019). Observations showing vesicles and pearl-like tubules at the region between the ER and Golgi in fat bodies and imaginal discs of flies were later reported using volume FIB-SEM (Yang et al., 2021). A cryo-tomography study of *Chlamydomonas reinhardtii* focused on the Golgi apparatus revealed multiple COPI-coated buds with dense, uniform coats at cisternal rims and CCs near the trans-Golgi network (TGN) regions (Bykov et al., 2017). Although not the primary focus, ERES adjacent to the Golgi contained slightly larger COPII-coated vesicles with a characteristic two-layered coat; however, no data were presented from other cellular regions. Taken together, these morphological observations support conclusions suggesting the existence of COPII-coated vesicular carriers, independently reached through numerous biochemical experiments conducted under diverse conditions, including analyses of partially and fully purified membranes and COPII component carriers. These findings contrast with earlier work (Mironov et al., 2003), which used chemically fixed samples under conditions of synchronized ER exit of a large cargo or membrane protein and reported an absence of vesicular intermediates, proposing instead that non-coated tubular carriers emerge directly from the ER.

Recently, concerns were raised about the interpretation of these structural studies supporting vesicle-mediated transport from ERES, citing potential limitations related to section thickness, limited sampling volume, and, in some cases, artifacts introduced by chemical fixation (Weigel et al., 2021). To address these issues, Lippincott-Schwartz and colleagues applied high-resolution volumetric FIB-SEM imaging at isotropic 4–8 nm resolution, using cells preserved by HPFS. They complemented this approach with correlative light EM using cryo-structured illumination (Hoffman et al., 2020). Observing cells undergoing synchronized cargo release in cells ectopically expressing cargo or COPII subunits, they concluded that only tubular and not vesicular carriers emerged from enlarged ER domains. They also reported a similar presence of tubular ERES and absence of vesicular ERES in non-transfected HeLa cells, challenging the classical model of COPII vesicles as the key transport intermediates for conventional cargo in mammalian cells.

We report here our effort to resolve this apparent contradiction by imaging cells devoid of ectopic expression and preserved by HPFS, using high-resolution volumetric FIB-SEM. We analyzed the 3D images aided by the ASEM pipeline, trained to independently recognize COPI vesicles and ER. This approach enabled reliable identification of 50–70-nm COPI-coated vesicles adjacent to the Golgi apparatus, as well as small vesicles located near the ER and spatially separated from the Golgi. These vesicles typically formed clusters of 3–40, adjacent to flattened ER cisternae, were slightly larger, had a different appearance from COPI vesicles, and appeared throughout the cell volume in all mammalian cell types examined. We refer to these assemblies as vesicular ERES.

Considering these observations, we reexamined the same FIB-SEM dataset of a HeLa cell lacking ectopic expression of COPII subunits or secretory cargo (Weigel et al., 2021). Analysis of the automated COSEM segmentation released to the COSEM repository after publication, visualized with Neuroglancer, a WebGL-based volumetric data viewer (https://github.com/google/neuroglancer), revealed that approximately two-thirds of the structures annotated as tubular ERES contain vesicle-rich regions. Together, these findings support the coexistence of both vesicular and tubular ERES architectures in mammalian cells.

Results

FIB-SEM imaging across cell types

We used volume FIB-SEM to image cells preserved by HPFS (Hoffman et al., 2020; Studer et al., 2008; Xu et al., 2021). Our dataset included two human astrocyte-derived SVG-A cells (SVG-A1 and SVG-A2), one immortalized mouse dendritic cell (MuTuDC), and a human-induced pluripotent stem cell (iPSC)-derived neuron (iN) cultured *in vitro* (Table S1). Volume images were acquired using crossbeam FIB-SEM at an isotropic resolution of 5 × 5 × 5 nm per voxel or an anisotropic voxel size of 2 × 2 × 1 nm. We also analyzed a volumetric dataset of the HeLa-2 cell from the COSEM project acquired with a custom-modified FIB-SEM at 4 × 4 × 5.24 nm (Weigel et al., 2021) (Table S1). Unless otherwise noted, we trained and applied our ASEM model (Gallusser et al., 2022) directly to raw FIB-SEM volumes and conducted all subsequent visual inspections and analyses on these datasets. In some cases, we examined FIB-SEM datasets acquired at 2 × 2 × 1 or 4 × 4 × 5.24 nm voxel size denoised with a novel algorithm we developed to be published elsewhere. All datasets and figures from this study are available for interactive 3D exploration in Neuroglancer. This format provides the most effective way to examine the complex volumetric architecture of ERES and associated organelles. Instructions for accessing and navigating the Neuroglancer datasets are provided in the manuscript, and we invite readers to use this resource to explore the data in detail.

Recognition and segmentation of COPI vesicles

COPI vesicles, which measure 50–70 nm in diameter, localize to the periphery of the Golgi apparatus. They mediate selective retrograde transport from the Golgi to the ER and support bidirectional trafficking between Golgi cisternae (Béthune and

Wieland, 2018). These vesicles are coated by COPI coatomers but lack a strongly electron-dense coat in FIB-SEM images of HPFS-preserved samples stained with OsO_4 and uranyl acetate. They are nonetheless readily distinguishable from nearby CCVs, which are slightly larger (70–90 nm) and have a prominent electron-dense coat (Gallusser et al., 2022).

Ground truth segmentations of COPI vesicles were generated by annotating COPI vesicles at the Golgi periphery in FIB-SEM images from SVG-A1 and SVG-A2 cells Fig. S1. We trained the ASEM model (Gallusser et al., 2022) using annotations from 42, 47, and 51 manually segmented COPI vesicles of 50–70 nm in diameter across three distinct regions of interest in SVG-A1 and 32 vesicles from a fourth region in SVG-A2. Annotated volumes ranged from 204 to 250 voxels in the x and y axes and 110 to 250 voxels along the z axis, providing sufficient context for accurate neural network segmentation. An independent set of 35 COPI vesicles within a 180 × 180 × 210 voxel region of SVG-A1 excluded from training was reserved for validation, as detailed in the Materials and methods section. Annotations were performed on datasets acquired at 5 nm voxel size using Neuroglancer and WEBKNOSSOS (Boergens et al., 2017).

The ASEM COPI model achieved a Dice coefficient of 0.8482 during training and 0.4176 for validation, with a final loss (binary cross entropy) of 0.0095 after 167,000 epochs (~21 h of training). Visual inspection confirmed accurate identification of COPI vesicles adjacent to the Golgi apparatus in the training and validation datasets, as well as other vesicles in additional regions not included in the training of the SVG-A, MuTuDC, iN and HeLa-2 cells (Figs. 1, 2, 3, 4, and 5; and Figs. S1, S2, and S3).

Detection of vesicular ERES

A second class of slightly larger vesicles, ~90–110 nm in diameter, characterized by a distinct electron-dense coat typical of CCVs and localized to the distal side of the TGN, was used as an internal control to test the specificity of the COPI model. While these vesicles were not recognized by our COPI ASEM model (Fig. 2), they were accurately identified by our clathrin-coat ASEM model (Fig. 2; and Videos 1, 2, 3, 4, 5, 6, 7, 8, 9, 10, 11, and 12), previously trained using ground truth annotations of endocytic clathrin-coated pits in plasma membrane images (Gallusser et al., 2022); likewise, the clathrin-coat ASEM model did not misidentify COPI vesicles (Fig. 2). These results illustrate the specificity and robustness of our COPI and clathrin coat models, underscoring the importance of tailored training for specific vesicle classes.

Identification of vesicular ERES

Additional vesicles, measuring ~50–90 nm in diameter, were identified by our ASEM COPI model across the cell volumes of non-transfected SVG-A, iN, and HeLa cells. Initial visual inspection using Neuroglancer showed that these vesicles were often located far from the Golgi apparatus (Fig. 1). They were typically members of small clusters of similar vesicles, of which only one or a few were detected by ASEM. We initially identified ~400 such sites in the partial volumes of SVG-A and iN cells and across a fraction of the full volume of the non-transfected HeLa-2 cell.

The high spatial density of organelles and vesicles ranging from small carriers to larger structures such as endosomes, mitochondria, and ER complicated the assignment of specific identities to the mapped vesicles. Thus, to aid in the visual interpretation and improve contextual characterization of the vesicles, we took advantage of the extensive distribution of the ER as a 3D spatial reference. Using our previously trained and validated ASEM ER segmentation model (Gallusser et al., 2022), we identified ER within the same cells. These vesicles, recognized by our ASEM COPI model and located away from the Golgi apparatus, were typically within ~120 nm of flattened, expanded ER cisternae. Detailed visual inspection of a random subset of 30 sites in SVG-A cells and 43 sites in HeLa cells revealed considerable variability in vesicle cluster sizes, ranging from 5 to 40 vesicles per cluster within volumes ~400 nm in all directions (Figs. 3 and S3). Vesicle diameters measured near the Golgi in SVG-A (59.2 ± 9.1 nm, n = 24) and HeLa (60.1 ± 8.0 nm, n = 24) cells were significantly smaller ($P < 0.0001$) than those near the ER in SVG-A (75.7 ± 9.1 nm, n = 24) and HeLa (75.9 ± 9.5 nm, n = 24) cells. These dimensions agree with prior measurements of the smaller COPI and larger COPII vesicles. Because the vesicles recognized by our COPI ASEM model spanned both size ranges, we used the segmentations as visual guides to identify regions of interest in the densely crowded FIB-SEM volumes.

Resolving COPI versus COPII vesicles at higher resolution

Since COPI and COPII vesicles differ in size, coat composition, and architecture, the ability to distinguish them directly in FIB-SEM images would be a significant advantage. However, prior studies using voxel sizes of 4–5 nm have not achieved this. We resolved this limitation by combining FIB-SEM acquisition at 2 × 2 × 1 nm voxel size with our novel denoising protocol (to be described elsewhere). Visual inspection of datasets from SVG-A (Fig. 4) and MuTuDC (Fig. S2) cells revealed differences between the smaller, densely stained COPI-coated vesicles near the Golgi and the broader size distribution, including larger vesicles with a clearer outline of the surrounded membrane associated with ribosome-free ER at ERES (blue arrow heads). The overall staining in the MuTuDC sample was denser, and the contrast in appearance between COPI and ER-associated vesicles was less pronounced (Fig. S2). We include an example from the SVG-A cell of vesicles in a closely apposed, concatenated arrangement, which, if not well resolved, could be misinterpreted as a continuous tubule (Fig. 4, B and C).

While we acknowledge that the current FIB-SEM data do not provide sufficient structural detail to directly assign molecular identity to the ER-associated vesicles, the available evidence supports a parsimonious interpretation. Given that COPI and COPII are the sole known coats associated with carriers related to the ER (see, for example, [Weigel et al., 2021; Chowdhury et al., 2020; Schröter et al., 2016]), we associate the vesicles observed at ERES with COPI and COPII, without inferring a specific state within the coating or uncoating cycle.

Comparison of vesicular and tubular ERES in HeLa cells

We further compared the positions of 247 vesicular ERES we identified in the HeLa-2 cell guided by the location of vesicles

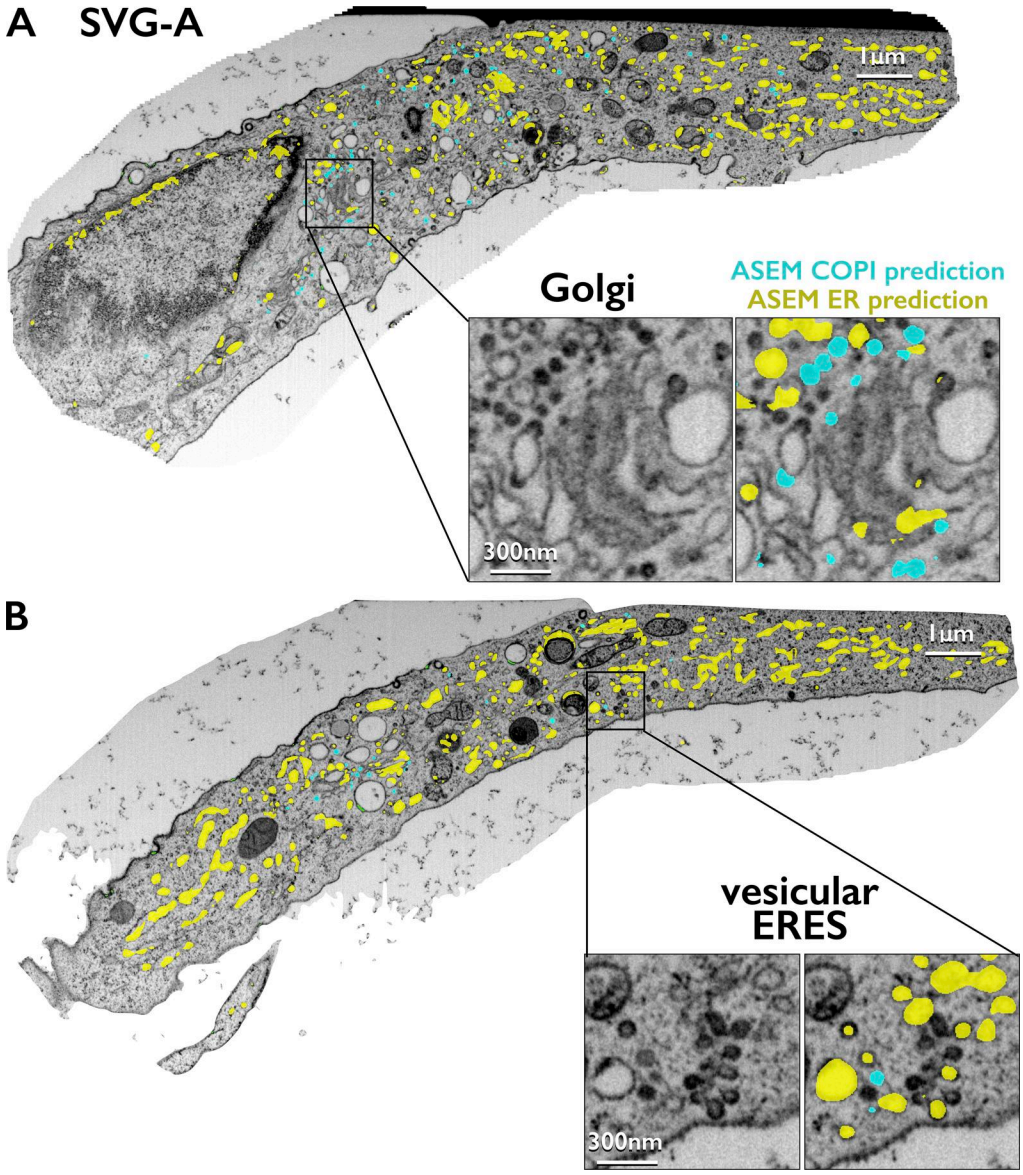

Figure 1. **FIB-SEM images and deep-learning neural networks ASEM predictions of ER and COPI vesicles. (A and B)** Single-plane views from a FIB-SEM volume image of a portion from an interphase SVG-A cell prepared by HPFS and visualized at 5-nm isotropic voxel size. Binary masks generated by the ASEM models for ER and COPI highlight predicted structures: yellow for the ER, light blue for COPI vesicles highlighting examples at a location near the Golgi apparatus corresponding to *bona fide* COP-I vesicles (A) and at a location adjacent to the ER for COPI-like vesicles assigned as part of the vesicular ERES (B). Predictive segmentations generated by the ASEM models served only as guides to identify regions of interest within the naïve FIB-SEM images and were not intended as precise segmentations. Scale bars: 1 µm and 300 nm in insets. Scale bars: 1 µm and 300 nm in insets.

identified to be in proximity of the ER with 779 tubular ERES annotated in the COSEM project dataset data acquired at 4 × 4 × 5.4 nm voxel size (Weigel et al., 2021), which employed an automated tubular ERES segmentation model not used in the original publication (Fig. S3). Our vesicular ERES showed no preferential distribution within the cell volume (Fig. S3 B). Among these, 179 vesicular ERES, containing vesicle clusters, were spatially distinct from 705 tubular ERES, highlighting heterogeneity in ERES organization. The remaining 68 vesicular ERES, each associated with 1–3 vesicles, localized adjacent to 74 tubular ERES, including instances where two vesicular ERES neighbored a single tubular ERES (Fig. S3, A–C).

Re-evaluation of tubular ERES annotations in COSEM dataset

Finally, we used Neuroglancer to reexamine the same HeLa-2 cell, denoised from the original 4 × 4 × 5.4 nm dataset, focusing on random sites annotated as tubular ERES by the model by Weigel et al. (2021). Many annotations corresponded to enlarged membrane varicosities, generic ER clusters, or vesicles (Fig. 5), with spatial arrangements resembling the vesicular ERES observed in SVGA, iNs, and MuTuDC cells. Notably, vesicle clusters appeared at approximately two-thirds of the sites annotated as tubular ERES.

In conclusion, our volumetric observations support a simple interpretation: mammalian ERES can consist of vesicle clusters, large vesicles with buds, or extended tubular structures.

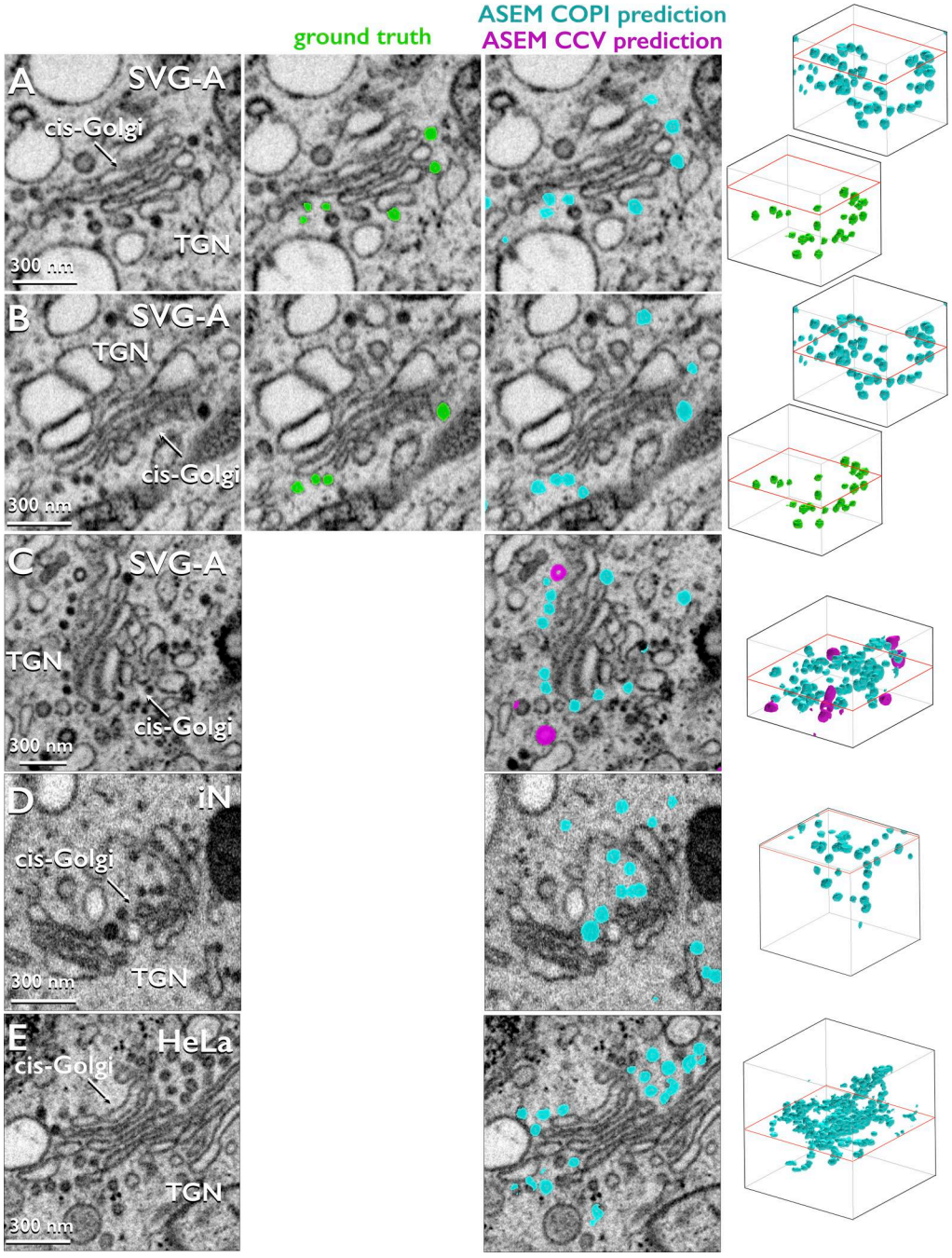

Figure 2. **ASEM predictions of COPI vesicles and CCVs near the Golgi apparatus (Associated with** Videos 1, 2, 3, and 4**). (A–E)** Left panels: Single-plane views from FIB-SEM volume images of the indicated cell types, prepared by HPFS and visualized during interphase at 5-nm isotropic voxel size. Central panels: Examples of ground truths used for training (A) and validation (B) for COPI vesicles (green) near the Golgi apparatus imaged at different planes of the same cell. Right panels: Predictions near the Golgi apparatus for COPI vesicles (light blue) and CCVs (CCV, magenta), generated by two different ASEM models trained with COPI and endocytic clathrin-coated pits, respectively. Scale bars: 300 nm. Rightmost panels: Volumetric renditions of the ground truths and ASEM predictions of COPI-coated vesicles and CCVs. Predictive segmentations generated by the ASEM models served only as guides to identify flattening regions of interest within the naïve FIB-SEM images and were not intended as precise segmentations.

Discussion

We present a unified description of the 3D architecture of ERES in mammalian cells, clarifying recent disagreements about the mechanisms underlying the earliest step of the secretory pathway. Specifically, we address the controversy regarding whether tubular or vesicular carriers mediate trafficking from the ER. We obtained high-resolution, isotropic, volume FIB-SEM images from various mammalian cell types preserved by HPFS. These datasets, independently acquired by our laboratory and the COSEM team at Janelia Research Campus, enabled comprehensive 3D reconstructions of this complex subcellular organization. Using automated segmentation powered by our deep-learning-

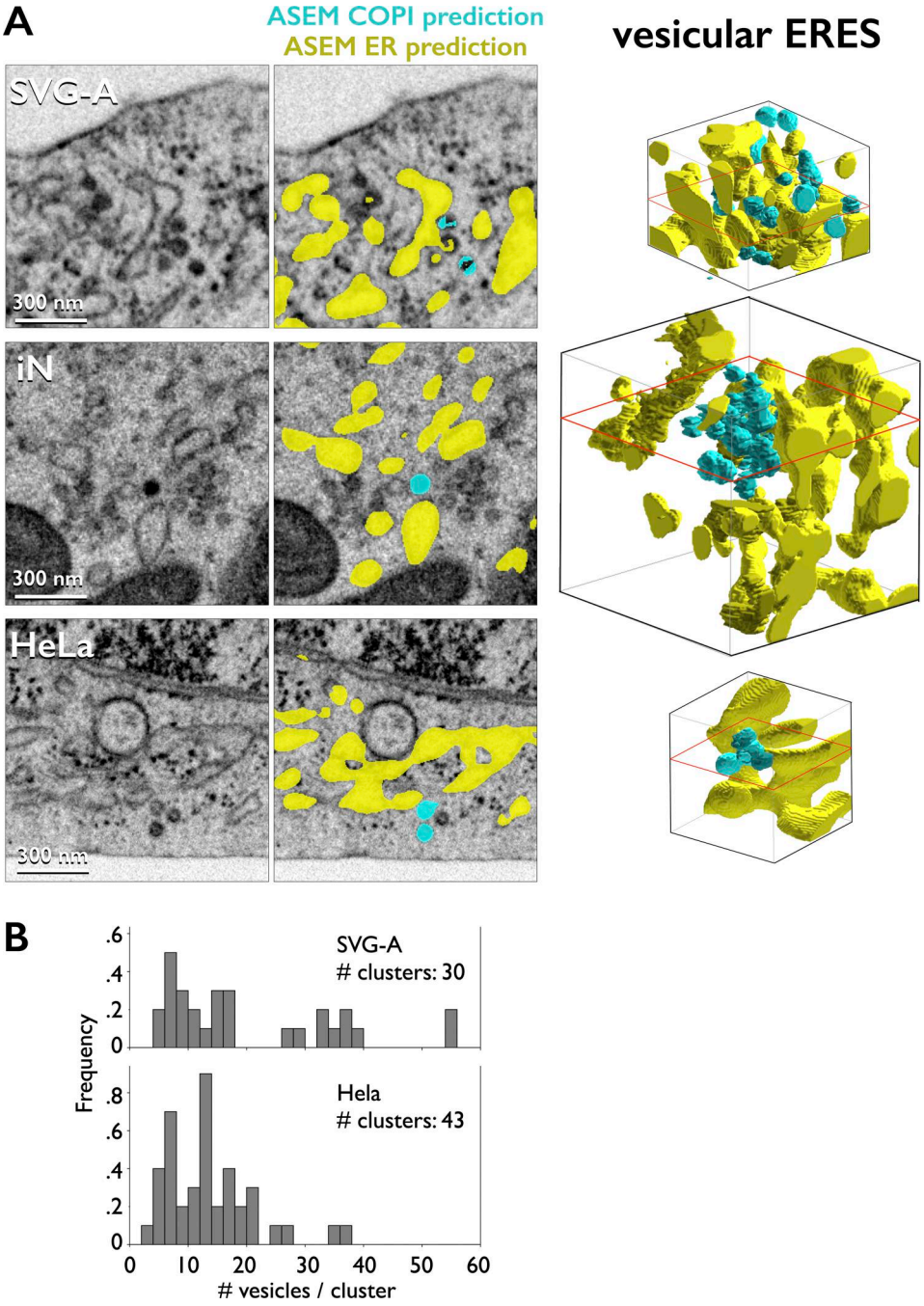

Figure 3. **Vesicular ERES (Associated with** Videos 5, 6, and 7**). (A)** Left panels: Single-plane views from FIB-SEM volume images of the indicated cell types, prepared by HPFS and visualized during interphase at 5-nm isotropic voxel size. Middle panels: ASEM model predictions of COPI-like vesicles (light blue) clustered near the predicted ER (yellow). Scale bars: 300 nm. Right panels: Manually annotated volumetric renditions of vesicles and ER in vesicular ERES. Predictive segmentations generated by the ASEM models served only as guides to identify regions of interest within the naïve FIB-SEM images and were not intended as precise segmentations. **(B)** Quantification of vesicular profiles per cluster at visually identified vesicular ERES sites.

based ASEM pipeline, trained to distinguish COPI vesicles from ER structures, we identified numerous small clusters of 50–70 nm COPI-like vesicles closely apposed to flattened ER cisternae. We have termed these clusters, presumably of COPII-coated vesicles, vesicular ERES. Our findings demonstrate that vesicular ERES coexist with tubular ERES—the latter comprising the tubular extensions previously proposed as exclusive transport carriers originating from the ER.

Our identification of vesicular ERES is consistent with earlier tomographic reconstructions from 250 to 300 nm thick sections imaged by TEM of cryo-protected samples of yeast (Mogelsvang et al., 2003; Levi et al., 2010) and plants (Donohoe et al., 2013) and of HpG2 cells immuno-gold labeled with an antibody specific for Sec23 and Sec 31 from COPII (Zeuschner et al., 2006). These observations also agree with the 3D architecture of vesicular ERES previously described as clusters of small vesicles adjacent

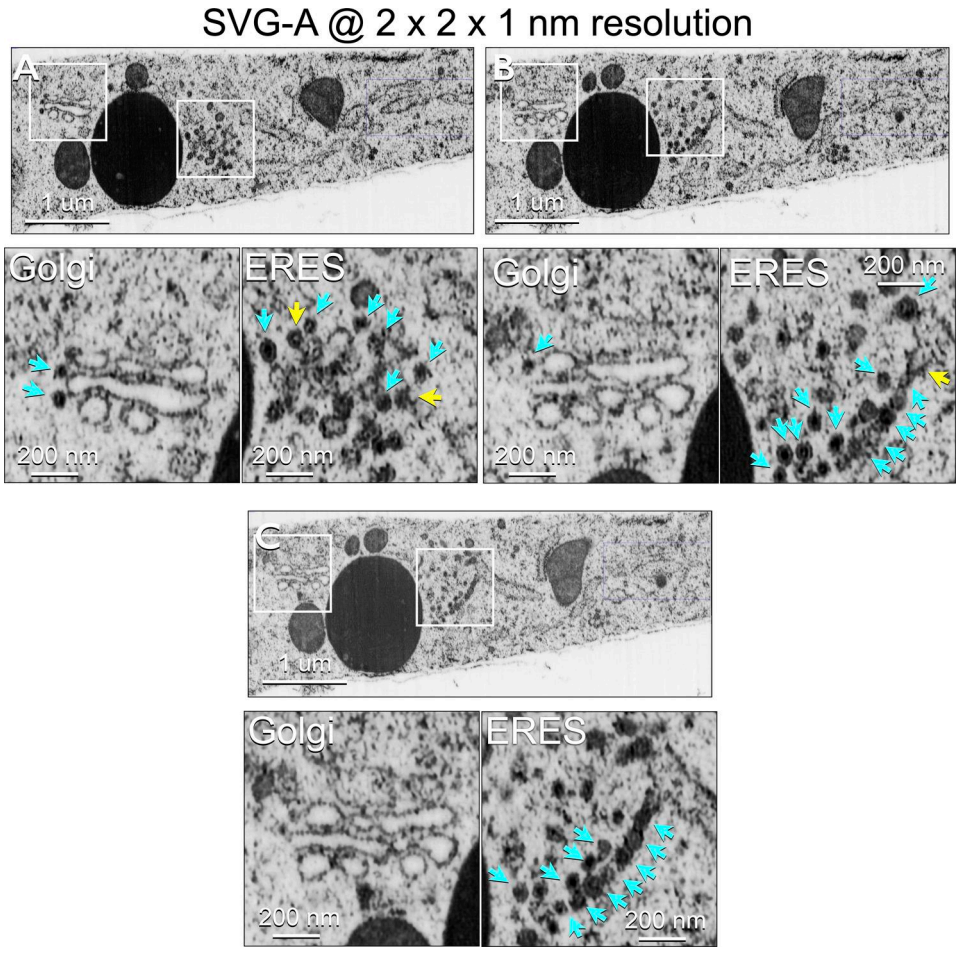

Figure 4. **COPI vesicles near the Golgi apparatus and vesicular ERES (Associated with Video 8).** Single-plane views from a denoised FIB-SEM volume of an interphase SVG-A cell acquired at 2 × 2 × 1 nm voxel size. Scale bar: 1 µm. Insets (3× enlargement, scale bar: 200 nm) show light blue arrowheads marking visually confirmed isolated COPI vesicles and associated ERES; yellow arrowheads indicate buds emanating from the ER. **(A–C)** correspond to z planes 384, 524, and 539, respectively. **(C)** Summary of spatial relationships between vesicular and tubular ERES shown in B. Among the 247 vesicular ERES, 179, each containing clusters of 5–50 vesicles and referred here as stand-alone vesicular ERES, were spatially distinct from the 779 tubular ERES annotated by the COSEM project. The remaining 68 vesicular ERES, each containing 1–3 vesicles, overlapped with 74 tubular ERES and are referred to as mixed ERES. No isolated vesicles identified by our ASEM COPI model were associated with the other 705 tubular ERES.

to enlarged ER cisternae in fat cells and imaginal discs from flies imaged using volume FIB-SEM (Yang et al., 2021). In that study, COPII-containing ER buds were shown adjacent to vesicles similarly decorated with COPII. Further support comes from cryogenic high-resolution electron tomography of INS-1 cells, imaged without fixation or staining, which revealed clear examples of coated ER buds adjacent to vesicular clusters containing both coated and uncoated vesicles (Carter et al., 2020). Although the structural resolution in these reconstructions was insufficient to definitively assign the coat composition, the arrangement is consistent with vesicular ERES.

Although broadly accepted, this model has been challenged by the alternative view that COPII facilitates cargo sorting at ERES but does not directly form transport vesicles (Mironov et al., 2003). Rather, COPII may remain at the ER membrane, not associating with cargo carriers moving toward the Golgi apparatus. Support for this hypothesis comes from live-cell fluorescence microscopy experiments showing fluorescently tagged COPII markers remaining stationary at ERES, while cargo-containing structures lacking COPII fluorescence move (Westrate et al., 2020; Hammond and Glick, 2000; Shomron et al., 2021). Furthermore, fluorescence recovery after photobleaching (FRAP) experiments indicated rapid exchange of COPII subunits between ERES-associated spots and the cytosol (Forster et al., 2006). It has also been suggested that stable COPII assemblies at ERES form tubular necks at the base of ER protrusions, which after membrane fission yield COPII-free tubular carriers traveling to the Golgi (Shomron et al., 2021). However, this interpretation faces limitations inherent to the resolution of fluorescence microscopy. The observed fluorescent spots were diffraction limited (~300 nm in the x/y plane, ~600 nm along the z axis), dimensions consistent with the optical point spread function. Consequently, these images could not reliably discriminate between COPII-coated buds or tubular necks and individual vesicles or vesicle clusters separated by distances of 300–400 nm, as demonstrated by higher-resolution EM from our studies and those of others (Carter et al., 2020;

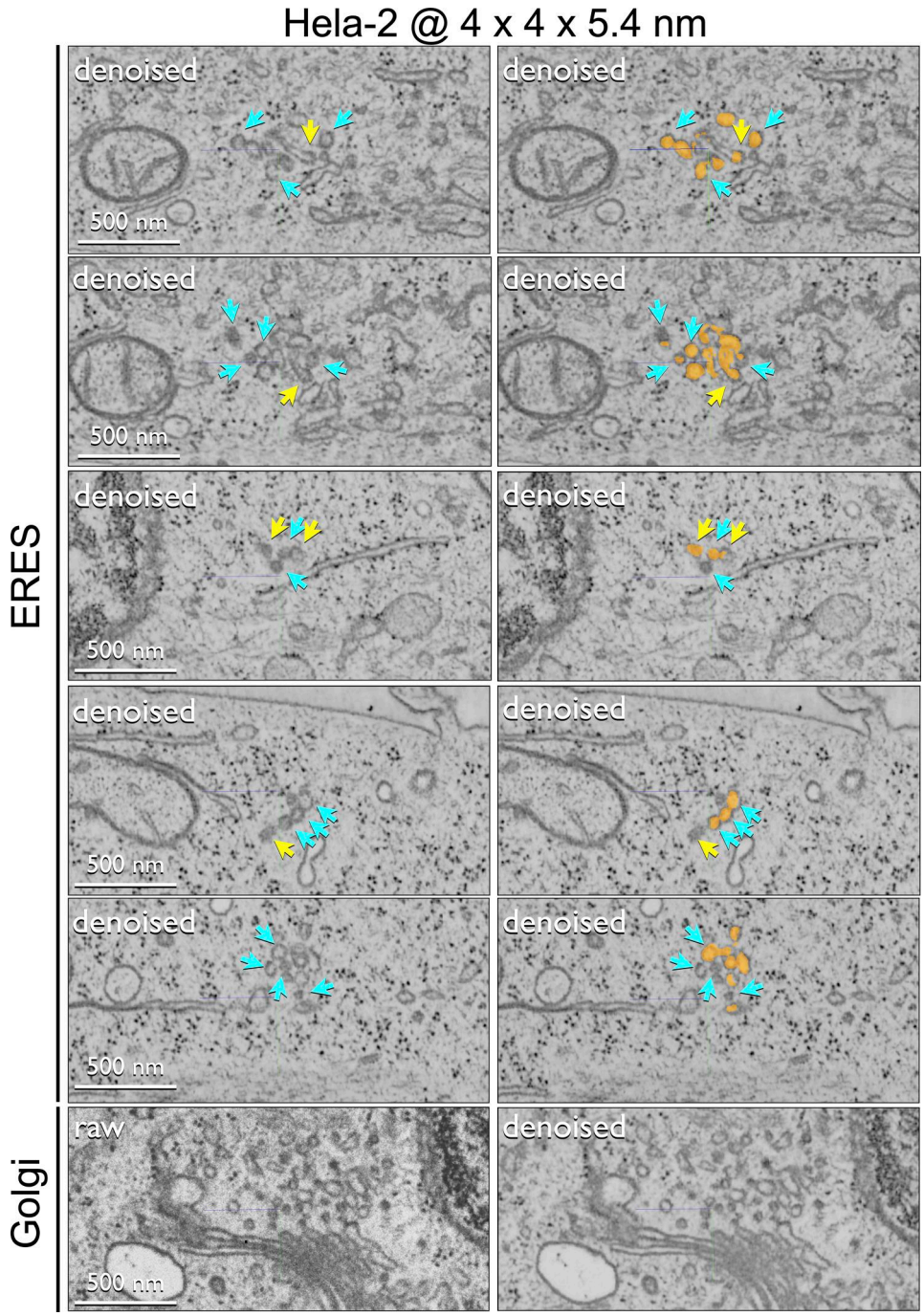

Figure 5. **Abundant vesicles at tubular ERES predicted by the COSEM project (associated with** Video 9**).** Single-plane views from a denoised FIB-SEM dataset of an interphase HeLa-2 cell prepared by HPFS, acquired at 4 × 4 × 5.24 nm voxel size. Images show randomly selected sites predicted as tubular ERES by the COSEM model (orange), highlighting abundant isolated vesicles (blue arrowheads) adjacent to tubular ER (yellow arrowheads), verified by visual inspection using Neuroglancer. A representative example near the Golgi apparatus comparing the original and denoised images is also shown. Plane coordinates (z, y, and x) in nanometers for the images, from top to bottom, are: (12,506, 5,348, and 77,460), (12,452, 5,348, and 37,460), (15,090, 4,028, and 16,276), (17,093, 4,059, and 13,111), (16,954, 4,969, and 13,431), and (13,724, 4,637, and 32,400), respectively. FIB-SEM images generated with Neuroglancer thin blue, and green lines indicate orientation. Scale bar: 500 nm. The orthogonal axes of the 3D images are color coded (blue, green, red).

Zeuschner et al., 2006; Yang et al., 2021). Thus, these experiments do not unequivocally distinguish whether the observed COPII dynamics reflect exchange between membrane-bound and cytosolic pools or represent rapid, asynchronous cycles of vesicle coating and uncoating within unresolved clusters.

To address these discrepancies, Weigel et al. (2021) combined cryo-structured illumination microscopy with high-resolution FIB-SEM imaging to morphologically characterize ERES, identified by fluorescently tagged COPII subunits and secretory cargo. Their FIB-SEM analysis, primarily conducted at 8 × 8 × 8

nm voxel size on HeLa cells overexpressing the fluorescent markers, concluded that tubular extensions alone defined ERES, excluding vesicular structures. However, reliance on colocalization with fluorescent COPII puncta could have inadvertently overlooked detection of vesicular ERES.

Our analysis using higher-voxel size FIB-SEM images (5 × 5 × 5 nm and denoised 2 × 2 × 1 nm) clearly revealed vesicular ERES in diverse mammalian cell types. Positional correlation analyses between tubular ERES identified with the ERES model by the COSEM team and vesicular ERES we detected in non-transfected HeLa cells confirm the coexistence of these distinct morphological entities. In alignment with earlier proposals, we propose that vesicular ERES primarily mediate the transport of relatively small cargo, whereas tubular ERES facilitate trafficking of larger cargo. Moreover, the morphological similarities between tubular ERES and vesicular-tubular clusters, which correspond to the ER-Golgi intermediate compartment (Nakano, 2022; Martínez-Menárguez et al., 1999), suggest that some tubular ERES might serve as sorting stations involved in both retrograde and anterograde traffic. Whether the different forms of ERES reflect distinct temporal stages in their biogenesis, or whether the ratio of tubular to vesicular ERES adjusts dynamically in response to increased cargo flux (Forster et al., 2006; Farhan et al., 2008) or to changes in cellular physiology, remains to be determined.

In conclusion, the most parsimonious model integrating the available morphological and cell biochemical data suggests that COPII assembles at specialized ER sites distributed throughout the cell, coordinating cargo capture and sorting with membrane deformation. This assembly process can result in either fully enclosed COPII-coated vesicles or partially assembled coats functioning as scaffolds for extended membrane carriers, such as the tubular structures observed in mammalian cells. Following vesicle formation, COPII rapidly disassembles, often before the vesicle has moved far from its ER membrane of origin, like the uncoating dynamics of endocytic CCVs and of CCVs originating from the TGN. The uncoated COPII vesicles and tubular carriers then traffic toward the Golgi apparatus along microtubules, guided by motor proteins.

Finally, our study highlights how high-resolution EM, applied at the cellular-volume scale, enables detailed structural insights from 3D imaging data. Our ASEM deep learning pipeline enabled accurate and efficient segmentation of vesicles and ER structures, used here as a tool to guide and facilitate visualization of the inherently complex subcellular architecture in its native spatial context. Importantly, our goal was not exhaustive identification of every vesicle, but rather to provide a reliable visual framework to know "where to look." We provide unrestricted access to our datasets and user-friendly tools developed for the ASEM pipeline. Our publicly available repository, https://open.quiltdata.com/b/asem-project, includes FIB-SEM volumes, training datasets, segmentation models and reconstructions, and our GitHub repository at https://github.com/kirchhausenlab/incasem, easily accessible open-source code. By making these resources freely available, we aim to enable the broader scientific community to explore, validate, and extend our findings, fostering further discoveries at the intersection of computational and cell biology.

Materials and methods

Cells

Growth conditions for mycoplasma-free human fetal immortalized astrocyte SVG-A cells and iNs were as described previously (Gallusser et al., 2022; Sanyal et al., 2024), (Gallusser et al. [Table S1]). Inmortalized MuTuDCs (Pigni et al., 2018) were a gift from the Hidde Ploegh laboratory; they were cultured in RPMI media (10-040-CM; Corning) supplemented with 8% FBS (S11150H; Atlanta Biologicals) and 50 µM of β-mercaptoethanol and incubated with 1 µg/ml of lipopolysaccharide prior to FIB-SEM imaging. Conditions for HeLa cells were described by Weigel et al. (2021).

HPFS and embedding

Procedures for HPFS and embedding of SVG-A cells and iNs were as described previously (Gallusser et al., 2022; Sanyal et al., 2024). Briefly, SVG-A cells were plated on 6 × 0.1-mm sapphire disks (616-100; Technotrade International; six disks per dish) and grown in MEM medium (10009CV; Corning) supplemented with 10% FBS (S11150; Atlanta Biologicals) (Sanyal et al., 2024). iNs were plated on 6 × 0.1-mm sapphire disks pre-coated with Matrigel as detailed by Sanyal et al. (2024). For freezing, two sapphire disks, one with cells, were separated by a 100-µm stainless steel spacer (1257-100; Technotrade) and processed using either a Leica EM ICE (Leica Microsystems; SVG-A cells) or Wohlwend HPF Compact 03 (Technotrade; iNs) high-pressure freezer. Frozen samples were transferred under liquid nitrogen to cryotubes containing frozen substitution medium (2% OsO_4, 0.1% uranyl acetate, and 3% water in acetone).

Freeze-substitution was performed in an EM AFS2 apparatus (Leica Microsystems) programmed for sequential warming: −140°C to −90°C (2 h), −90°C for 24 h, −90°C to 0°C (12 h), and 0°C to 22°C (1 h). Samples on sapphire disks were sequentially rinsed three times with anhydrous acetone, propylene oxide (Electron Microscopy Sciences), and 50% resin (Embed 812 mix; EMS 14121) in propylene oxide. Disks were then transferred into embedding molds (EMS 70900) containing 100% resin and polymerized at 65°C for 48 h. After polymerization, sapphire disks were removed from the resin blocks by sequential immersion in liquid nitrogen and boiling water.

Crossbeam FIB-SEM isotropic imaging

As previously described (Gallusser et al., 2022), polymerized resin blocks were removed from molds and mounted onto aluminum pin stubs (Ted Pella) with conductive silver epoxy (EPO-TEK H20S, EMS), exposing the free face. The exposed face was carbon coated (20 nm) using a Quorum Q150R ES sputter coater (Quorum Technologies) and loaded into a Zeiss Crossbeam 540 microscope for FIB-SEM imaging. After eucentric correction, the stage was tilted to 54° with a working distance of 5 mm for beam alignment. Following SEM localization of the cell of interest, a platinum protective layer was deposited by gas injection. A coarse trench adjacent to the cell was milled with a 30 kV/30 nA gallium ion beam, and the exposed block face was polished at 30 kV/7 nA.

Sequential imaging employed interlaced milling (30 kV/3 nA gallium beam) and SEM imaging (1.5 kV/400 pA) at 5-nm intervals, yielding isotropic voxels (5 nm in X/Y/Z) or SEM imaging

(1.5 kV/800 pA) at 1-nm intervals for anisotropic voxels (2 × 2 × 1 nm in X/Y/Z). Registration marks were created atop the platinum layer with a 1.5 kV/50 pA gallium beam, enhanced by 1.5 kV/5 nA electron irradiation, followed by a secondary platinum coating. FIB-SEM images captured at 5 × 5 × 5 or 2 × 2 × 1 nm represented averaged signals from the in-lens secondary electron and backscattered electron ESB detectors, captured with a pixel dwell time of 10–15 or 1–2 µs, respectively. Sequential z-plane images were aligned using the Fiji plugin Register Virtual Stack Slices (https://imagej.net/plugins/register-virtual-stack-slices) with translation and shrinkage constraints (Schroeder et al., 2021).

Denoising of FIB-SEM images

We implemented a denoising strategy we named FastFIB, a self-supervised denoising approach based on the Noise2Noise paradigm (Lehtinen et al., 2018, *Preprint*), which trains a neural network to predict one noisy measurement from another, assuming both share an underlying signal. Because the network cannot reconstruct the uncorrelated noise, it learns to suppress it, yielding a cleaner output. In our case, the training pairs consisted of corresponding 3D subvolumes from FIB-SEM datasets acquired with in-lens and ESB detectors.

FastFIB uses a 3D U-Net architecture with four levels of depth and ∼10 million trainable parameters. The loss function was the Charbonnier loss, defined with $\alpha = 0.5$ and $\varepsilon = 1 \times 10^{-3}$. Prior to computing the loss, we applied a mild 3D Gaussian blur to the U-Net output. This procedure encouraged the network to produce slightly deblurred outputs, as the blurred version had to match the target. To further regularize the output, we penalized the spatial gradients of the difference between the raw output and its blurred counterpart, promoting smoothness and suppressing high-frequency noise.

We trained the model on two datasets: one we acquired at isotropic 5 × 5 × 5 nm voxel size and the other at anisotropic 2 × 2 × 1 nm voxel size. Before training, we upsampled the latter to 1 × 1 × 1 nm using trilinear interpolation to enforce isotropy.

After training, we performed brief fine-tuning on our FIB-SEM data acquired from 5 × 5 × 5 or 2 × 2 × 1 nm data that had not been used for training, which modestly improved the network's performance on these inputs. We also applied the trained 5 × 5 × 5 nm FastFIB model directly to the 4 × 4 × 5.24 nm FIB-SEM dataset of a HeLa cell from the COSEM project. Because this dataset included only in-lens detector data, no retraining was performed.

Annotations

COPI vesicles

Ground truth manual annotations for selected COPI vesicles (50–70 nm diameter) adjacent to the Golgi apparatus in SVG-A cells were performed approximately every third plane, followed by automatic volumetric completion using WEBKNOSSOS (Boergens et al., 2017). Binary masks were created at least 47 voxels from the edges of the 3D FIB-SEM images from three regions adjacent to the TGN in SVG-A1 cells, containing 42, 47, and 51 vesicles, respectively, and one region in SVG-A2 cells with 32 vesicles. Dimensions of the training regions were 204 × 204 × 204, 110 × 250 × 250, and 225 × 225 × 225 voxels in SVG-A1 and 225 × 225 × 225 voxels in SVG-A2; dimensions of the validation region in SVG-A1 were 180 × 180 × 210 voxels.

Dispersed COPI-like vesicles and vesicular ERES

The COPI ASEM model trained with the selected COPI vesicles identified numerous vesicles in naïve regions of the SVG-A cells not used for training. To catalog these, voxels labeled as positive within 60 nm were grouped into single objects (e.g., 331 vesicles). Visual inspection revealed many of these as *bona fide* COPI vesicles clustered near the Golgi apparatus (Fig. 2). Vesicles in regions >400 nm or within 320 nm in any dimension were computationally excluded, leaving 273 dispersed vesicles throughout the cell. Of these, visual inspection of the 247 identified objects were individually or occasionally paired vesicles clustered with similar vesicles undetected by the COPI ASEM model.

We calculated the shortest geometric distance between these vesicles and ER structures segmented using our ER ASEM model, identifying 247 vesicles within 120 nm of the ER, designated vesicular ERES. We calculated the distance between the vesicle membrane and the ER by applying the Pythagorean theorem in three dimensions to coordinates obtained by visual inspection. Neuroglancer-based visual inspection confirmed that 179 vesicles belonged to clusters of 5–55 vesicles in regions ≤400 nm, while the remaining 68 appeared as isolated vesicles near tubular ERES identified by the COSEM project (Fig. S3).

Relationship between vesicular and tubular ERES in the HeLa-2 cell

To compare vesicular ERES identified by the COPI ASEM model with tubular ERES defined by the COSEM project in the HeLa-2 cell, FIB-SEM data were analyzed as follows: (1) Voxels labeled as positive by the COSEM ERES model were grouped into single objects if they were within 140 nm of each other ($n = 779$), a threshold selected based on visual inspection due to larger predicted tubular ERES sizes. (2) X/Y/Z coordinates of 247 vesicular ERES predicted by the COPI ASEM model were compared with coordinates of tubular ERES from the COSEM ERES model to identify vesicles located within 50 nm. (3) Predictions were classified into isolated vesicular ERES ($n = 179$), vesicular ERES associated with one ($n = 68$) or two ($n = 6$) tubular ERES, and isolated tubular ERES ($n = 705$). Classification accuracy was confirmed by visual inspection using Neuroglancer.

Computational requirements for training and predictions

Data fetching and augmentation were executed in parallel using eight CPU cores, and training was performed on a single NVIDIA DGX-A100 GPU. Each iteration of the ASEM neural network training required ∼1 s, with total training durations typically ranging from 100,000 to 170,000 iterations (∼20–30 h, including validation). Predictions performed using 100 workers, processing input and output volumes of 364 × 364 × 364 voxels and 270 × 270 × 270 voxels, respectively, required ∼8 min per single-cell image stack.

Model training and predictions

COPI vesicles

The ASEM COPI model training using FIB-SEM data from SVG-A1 cells converged after 167,000 iterations, achieving a Dice

coefficient of 0.392 and a loss function (binary cross entropy) value of 0.008. Visual inspection using Neuroglancer of predicted segmentations (~4.08 billion cubic voxels), which were not part of the training set, confirmed accurate identification of *bona fide* COPI vesicles adjacent to the Golgi and COPI-like vesicles distant from the Golgi. These segmentations represented vesicles with diameters of 50–80 nm, alone or as clusters of 2–7. Similar accuracy was observed upon applying the COPI ASEM model to iN and HeLa cell datasets not used during training.

CCVs

Previously, we demonstrated the efficacy of the clathrin-coated pit ASEM model trained on endocytic clathrin-coated pits for identifying CCVs near the cell surface and distal side of the TGN (Table S1, cells 12 and 13 [Gallusser et al., 2022]). Using this model, we predicted CCVs in the SVG-A1 cell. Neuroglancer-based visual inspection verified these predictions, identifying vesicles near the TGN ranging in diameter from 110 to 130 nm and clearly distinct from COPI vesicles detected by the COPI ASEM model.

Statistical analysis

The FIB-SEM samples from different cell types are biological replicates, e.g., fully processed independently of each other. Because the study focuses on the description of nonquantifiable morphological features, statistical testing is not applicable and was not applied.

Online supplemental material

Supplementary figures provide additional methodological details and validation. Fig. S1 outlines the workflow for training and application of ASEM models to FIB-SEM datasets. Fig. S2 presents denoised FIB-SEM planes highlighting COPI vesicles near the Golgi apparatus and vesicular ERES in MuTuDC cells. Fig. S3 compares vesicular and tubular ERES in the HeLa-2 COSEM dataset, including ASEM predictions and volumetric renditions. Supplementary videos illustrate annotated 3D renderings of vesicles and ERES from FIB-SEM datasets. Videos 1, 2, 3, and 4 show COPI-coated vesicles and CCVs adjacent to the Golgi apparatus in SVG-A, iN, and HeLa cells. Videos 5, 6, and 7 highlight COPII vesicles at vesicular ERES adjacent to ER in SVG-A, iN, and HeLa cells. Videos 8 and 9 present COPI and COPII vesicles in SVG-A and MuTuDC cells, rendered in Imaris. Videos 10, 11, and 12 compare vesicular, tubular, and mixed ERES in the HeLa-2 dataset, annotated using WEBKNOSSOS. Table S1 summarizes the cells and datasets used in this study. It includes SVG-A cells imaged at 5 × 5 × 5 nm voxel size (Cell IDs #81, #84), iNs at 5 × 5 × 5 nm (Cell ID #131), and a HeLa-2 cell acquired by the COSEM project at 4 × 4 × 5.24 nm (Cell ID #3E). For each dataset, details of preparation, contributors, voxel resolution, and public access links are provided.

Data availability

The datasets of raw FIB-SEM cell images, ground truth annotations, probability maps predicted by the models, and corresponding segmentation masks are publicly available at the AWS ASEM bucket: https://open.quiltdata.com/b/asem-project. An online publicly available tool based on Neuroglancer has been created to view 3D volumes relevant to this study and others. The tool is available at https://asem-viewer-env.eba-rrnvmfwa.us-east-1.elasticbeanstalk.com/ and allows users to quickly select and visualize cells and volumes (raw data, prediction results, and ground truth labels). The ASEM pipeline software and step-by-step usage instructions are publicly available at https://github.com/kirchhausenlab/incasem (ASEM deep learning pipeline). Users comfortable with Linux and who have access to an NVIDIA GPU should follow the standard installation and usage instructions from GitHub. For users with limited experience in these areas or without a GPU, we provide two alternatives to facilitate usage. Option 1: A Google Colab notebook, available as ASEM_Notebook.ipynb, provides a cloud-based alternative that eliminates the need for a local installation. The notebook can be accessed from the Interactive Demo section of the README.md in the incasem GitHub. This option is ideal for users who wish to explore ASEM as a demo and access cloud-hosted GPUs. Note that a Colab membership may be required for extended use. Option 2: Through the GitHub installation, users can run incasem in command-line mode or via a GUI that assists with configuring and launching training, fine-tuning, and predictions. For access details, see the UI Installationsection of README.md in the incasem GitHub. Trained neural network models are available at https://open.quiltdata.com/b/asem-project, with usage instructions provided at https://github.com/kirchhausenlab/incasem. The model used to detect COPI vesicles for the primary analysis is 2631.

Acknowledgments

We thank J. O'Connor for his help setting up and maintaining the computing infrastructure and the members of the Kirchhausen laboratory for their help and encouragement.

The research was supported by a National Institute of General Medical Sciences Maximizing Investigators' Research Award GM130386 and by the NNF Center of Optimized Oligo Escape and Control of Disease awarded to Tom Kirchhausen and N. Hatzakis. Athul Nair and Akhil Nair were supported in part by discretionary funds available to Tom Kirchhausen. Acquisition of the FIB-SEM microscope was supported by a generous grant from Biogen to Tom Kirchhausen, and the high-pressure freeze substitution device was made available by S.C. Harrison. Acquisition of the computing hardware, including the DGX's GPU-based computers, CPU clusters, fast access memory, archival servers, and workstations that made possible this study, was supported by generous grants from the Massachusetts Life Sciences Center to T. Kirchhausen and by an equipment supplement to the National Institute of General Medical Sciences Maximizing Investigators' Research Award GM130386. Construction of the server room housing the computing hardware was made possible with generous support from the PCMM Program at Boston Children's Hospital.

Author contributions: Athul Nair: data curation, formal analysis, investigation, methodology, software, validation, visualization, writing—review and editing. Akhil Nair: data

curation, formal analysis, investigation, methodology, software, validation, visualization, and writing—review and editing. Patrick Stock: data curation, formal analysis, investigation, software, validation, and writing—review and editing. Arkash Jain: software. Elliott Somerville: investigation, resources, visualization, and writing—review and editing. Anwesha Sanyal: investigation and resources. Jose Inacio Costa-Filho: data curation, formal analysis, investigation, methodology, resources, software, validation, visualization, and writing—review and editing. Tom Kirchhausen: conceptualization, data curation, formal analysis, funding acquisition, investigation, methodology, project administration, supervision, validation, visualization, and writing—original draft, review, and editing.

Disclosures: The authors declare no competing interests exist.

Submitted: 1 May 2025
Revised: 16 July 2025
Accepted: 1 October 2025

References

Arzt, M., J. Deschamps, C. Schmied, T. Pietzsch, D. Schmidt, P. Tomancak, R. Haase, and F. Jug. 2022. LABKIT: Labeling and segmentation toolkit for big image data. *Front. Comput. Sci.* 4:777728. https://doi.org/10.3389/fcomp.2022.777728

Balch, W.E., J.M. McCaffery, H. Plutner, and M.G. Farquhar. 1994. Vesicular stomatitis virus glycoprotein is sorted and concentrated during export from the endoplasmic reticulum. *Cell*. 76:841–852. https://doi.org/10.1016/0092-8674(94)90359-x

Béthune, J., and F.T. Wieland. 2018. Assembly of COPI and COPII vesicular coat proteins on membranes. *Annu. Rev. Biophys.* 47:1–21. https://doi.org/10.1146/annurev-biophys-070317-033259

Boergens, K.M., M. Berning, T. Bocklisch, D. Bräunlein, F. Drawitsch, J. Frohnhofen, T. Herold, P. Otto, N. Rzepka, T. Werkmeister, et al. 2017. webKnossos: Efficient online 3D data annotation for connectomics. *Nat. Methods*. 14:691–694. https://doi.org/10.1038/nmeth.4331

Bykov, Y.S., M. Schaffer, S.O. Dodonova, S. Albert, J.M. Plitzko, W. Baumeister, B.D. Engel, and J.A. Briggs. 2017. The structure of the COPI coat determined within the cell. *Elife*. 6:e32493. https://doi.org/10.7554/elife.32493

Carter, S.D., C.M. Hampton, R. Langlois, R. Melero, Z.J. Farino, M.J. Calderon, W. Li, C.T. Wallace, N.H. Tran, R.A. Grassucci, et al. 2020. Ribosome-associated vesicles: A dynamic subcompartment of the endoplasmic reticulum in secretory cells. *Sci. Adv.* 6:eaay9572. https://doi.org/10.1126/sciadv.aay9572

Donohoe, B.S., B.-H. Kang, M.J. Gerl, Z.R. Gergely, C.M. McMichael, S.Y. Bednarek, and L.A. Staehelin. 2013. Cis-Golgi cisternal assembly and biosynthetic activation occur sequentially in plants and algae. *Traffic*. 14:551–567. https://doi.org/10.1111/tra.12052

Farhan, H., M. Weiss, K. Tani, R.J. Kaufman, and H.-P. Hauri. 2008. Adaptation of endoplasmic reticulum exit sites to acute and chronic increases in cargo load. *EMBO J.* 27:2043–2054. https://doi.org/10.1038/emboj.2008.136

Forster, R., M. Weiss, T. Zimmermann, E.G. Reynaud, F. Verissimo, D.J. Stephens, and R. Pepperkok. 2006. Secretory cargo regulates the turnover of COPII subunits at single ER exit sites. *Curr. Biol.* 16:173–179. https://doi.org/10.1016/j.cub.2005.11.076

Galbraith, C.G. 2023. Pumping up the volume. *J. Cell Biol.* 222:e202212042. https://doi.org/10.1083/jcb.202212042

Gallusser, B., G. Maltese, G.D. Caprio, T.J. Vadakkan, A. Sanyal, E. Somerville, M. Sahasrabudhe, J. O'Connor, M. Weigert, and T. Kirchhausen. 2022. Deep neural network automated segmentation of cellular structures in volume electron microscopy. *J. Cell Biol.* 222:e202208005. https://doi.org/10.1083/jcb.202208005

Gorur, A., L. Yuan, S.J. Kenny, S. Baba, K. Xu, and R. Schekman. 2017. COPII-coated membranes function as transport carriers of intracellular procollagen I. *J. Cell Biol.* 216:1745–1759. https://doi.org/10.1083/jcb.201702135

Hammond, A.T., and B.S. Glick. 2000. Dynamics of transitional endoplasmic reticulum sites in vertebrate cells. *Mol. Biol. Cell*. 11:3013–3030. https://doi.org/10.1091/mbc.11.9.3013

Heinrich, L., D. Bennett, D. Ackerman, W. Park, J. Bogovic, N. Eckstein, A. Petruncio, J. Clements, S. Pang, C.S. Xu, et al. 2021. Whole-cell organelle segmentation in volume electron microscopy. *Nature*. 599:141–146. https://doi.org/10.1038/s41586-021-03977-3

Hoffman, D.P., G. Shtengel, C.S. Xu, K.R. Campbell, M. Freeman, L. Wang, D.E. Milkie, H.A. Pasolli, N. Iyer, J.A. Bogovic, et al. 2020. Correlative three-dimensional super-resolution and block-face electron microscopy of whole vitreously frozen cells. *Science*. 367:eaaz5357. https://doi.org/10.1126/science.aaz5357

Knott, G., H. Marchman, D. Wall, and B. Lich. 2008. Serial section scanning electron microscopy of adult brain tissue using focused ion beam milling. *J. Neurosci.* 28:2959–2964. https://doi.org/10.1523/jneurosci.3189-07.2008

Ladinsky, M.S., J.R. Kremer, P.S. Furcinitti, J.R. McIntosh, and K.E. Howell. 1994. HVEM tomography of the trans-Golgi network: Structural insights and identification of a lace-like vesicle coat. *J. Cell Biol.* 127:29–38. https://doi.org/10.1083/jcb.127.1.29

Lehtinen, J., J. Munkberg, J. Hasselgren, S. Laine, T. Karras, M. Aittala, and T. Aila. 2018. Noise2Noise: Learning image restoration without clean data. *arXiv*. https://doi.org/10.48550/arxiv.1803.04189 (Preprint posted March 12, 2018).

Levi, S.K., D. Bhattacharyya, R.L. Strack, J.R. Austin, and B.S. Glick. 2010. The yeast GRASP Grh1 colocalizes with COPII and is dispensable for organizing the secretory pathway. *Traffic*. 11:1168–1179. https://doi.org/10.1111/j.1600-0854.2010.01089.x

Martínez-Menárguez, J.A., H.J. Geuze, J.W. Slot, and J. Klumperman. 1999. Vesicular tubular clusters between the ER and Golgi mediate concentration of soluble secretory proteins by exclusion from COPI-coated vesicles. *Cell*. 98:81–90. https://doi.org/10.1016/s0092-8674(00)80608-x

Mekuč, M.Ž., C. Bohak, E. Boneš, S. Hudoklin, R. Romih, and M. Marolt. 2022. Automatic segmentation and reconstruction of intracellular compartments in volumetric electron microscopy data. *Comput. Meth Prog. Bio.* 223:106959. https://doi.org/10.1016/j.cmpb.2022.106959

Mironov, A.A., A.A. Mironov, G.V. Beznoussenko, A. Trucco, P. Lupetti, J.D. Smith, W.J.C. Geerts, A.J. Koster, K.N.J. Burger, M.E. Martone, et al. 2003. ER-to-Golgi Carriers Arise through Direct En Bloc Protrusion and Multistage Maturation of Specialized ER Exit Domains. *Dev. Cell*. 5:583–594. https://doi.org/10.1016/s1534-5807(03)00294-6

Mogelsvang, S., N. Gomez-Ospina, J. Soderholm, B.S. Glick, and L.A. Staehelin. 2003. Tomographic evidence for continuous turnover of Golgi cisternae in Pichia pastoris. *Mol. Biol. Cell*. 14:2277–2291. https://doi.org/10.1091/mbc.e02-10-0697

Müller, A., D. Schmidt, C.S. Xu, S. Pang, J.V. D'Costa, S. Kretschmar, C. Münster, T. Kurth, F. Jug, M. Weigert, et al. 2020. 3D FIB-SEM reconstruction of microtubule–organelle interaction in whole primary mouse β cells. *J. Cell Biol.* 220:e202010039. https://doi.org/10.1083/jcb.202010039

Nakano, A. 2022. The golgi apparatus and its next-door neighbors. *Front. Cell Dev. Biol.* 10:884360. https://doi.org/10.3389/fcell.2022.884360

Narayan, K., C.M. Danielson, K. Lagarec, B.C. Lowekamp, P. Coffman, A. Laquerre, M.W. Phaneuf, T.J. Hope, and S. Subramaniam. 2014. Multi-resolution correlative focused ion beam scanning electron microscopy: Applications to cell biology. *J. Struct. Biol.* 185:278–284. https://doi.org/10.1016/j.jsb.2013.11.008

Parlakgül, G., A.P. Arruda, S. Pang, E. Cagampan, N. Min, E. Güney, G.Y. Lee, K. Inouye, H.F. Hess, C.S. Xu, and G.S. Hotamışlıgil. 2022. Regulation of liver subcellular architecture controls metabolic homeostasis. *Nature*. 603:736–742. https://doi.org/10.1038/s41586-022-04488-5

Pigni, M., D. Ashok, M. Stevanin, and H. Acha-Orbea. 2018. Establishment and characterization of a functionally competent type 2 conventional dendritic cell line. *Front. Immunol.* 9:1912. https://doi.org/10.3389/fimmu.2018.01912

Raote, I., and V. Malhotra. 2019. Protein transport by vesicles and tunnels. *J. Cell Biol.* 218:737–739. https://doi.org/10.1083/jcb.201811073

Roy Chowdhury, S., C. Bhattacharjee, J.C. Casler, B.K. Jain, B.S. Glick, and D. Bhattacharyya. 2020. ER arrival sites associate with ER exit sites to create bidirectional transport portals. *J. Cell Biol.* 219:e201902114. https://doi.org/10.1083/jcb.201902114

Sanyal, A., G. Scanavachi, E. Somerville, A. Saminathan, A. Nair, R.F. Bango Da Cunha Correia, B. Aylan, E. Sitarska, A. Oikonomou, N.S. Hatzakis, and T. Kirchhausen. 2025. Neuronal constitutive endolysosomal

perforations enable α-synuclein aggregation by internalized PFFs. *J. Cell Biol.* 224:e202401136. https://doi.org/10.1083/jcb.202401136

Schroeder, A.B., E.T.A. Dobson, C.T. Rueden, P. Tomancak, F. Jug, and K.W. Eliceiri. 2021. The ImageJ ecosystem: Open-source software for image visualization, processing, and analysis. *Protein Sci.* 30:234–249. https://doi.org/10.1002/pro.3993

Schröter, S., S. Beckmann, and H.D. Schmitt. 2016. ER arrival sites for COPI vesicles localize to hotspots of membrane trafficking. *EMBO J.* 35: 1935–1955. https://doi.org/10.15252/embj.201592873

Shomron, O., I. Nevo-Yassaf, T. Aviad, Y. Yaffe, E.E. Zahavi, A. Dukhovny, E. Perlson, I. Brodsky, A. Yeheskel, M. Pasmanik-Chor, et al. 2021. COPII collar defines the boundary between ER and ER exit site and does not coat cargo containers. *J. Cell Biol.* 220:e201907224. https://doi.org/10.1083/jcb.201907224

Studer, D., B.M. Humbel, and M. Chiquet. 2008. Electron microscopy of high pressure frozen samples: Bridging the gap between cellular ultrastructure and atomic resolution. *Histochem. Cell Biol.* 130:877–889. https://doi.org/10.1007/s00418-008-0500-1

Weigel, A.V., C.-L. Chang, G. Shtengel, C.S. Xu, D.P. Hoffman, M. Freeman, N. Iyer, J. Aaron, S. Khuon, J. Bogovic, et al. 2021. ER-to-Golgi protein delivery through an interwoven, tubular network extending from ER. *Cell*. 184:2412–2429.e16. https://doi.org/10.1016/j.cell.2021.03.035

Westrate, L.M., M.J. Hoyer, M.J. Nash, and G.K. Voeltz. 2020. Vesicular and uncoated Rab1-dependent cargo carriers facilitate ER to Golgi transport. *J. Cell Sci.* 133:jcs239814. https://doi.org/10.1242/jcs.239814

Wu, Y., C. Whiteus, C.S. Xu, K.J. Hayworth, R.J. Weinberg, H.F. Hess, and P. De Camilli. 2017. Contacts between the endoplasmic reticulum and other membranes in neurons. *Proc. Natl. Acad. Sci. USA*. 114:E4859–E4867. https://doi.org/10.1073/pnas.1701078114

Xu, C.S., K.J. Hayworth, Z. Lu, P. Grob, A.M. Hassan, J.G. García-Cerdán, K.K. Niyogi, E. Nogales, R.J. Weinberg, and H.F. Hess. 2017. Enhanced FIB-SEM systems for large-volume 3D imaging. *Elife*. 6:e25916. https://doi.org/10.7554/elife.25916

Xu, C.S., S. Pang, G. Shtengel, A. Müller, A.T. Ritter, H.K. Hoffman, S.-Y. Takemura, Z. Lu, H.A. Pasolli, N. Iyer, et al. 2021. An open-access volume electron microscopy atlas of whole cells and tissues. *Nature*. 599: 147–151. https://doi.org/10.1038/s41586-021-03992-4

Yang, K., M. Liu, Z. Feng, M. Rojas, L. Zhou, H. Ke, and J.C. Pastor-Pareja. 2021. ER exit sites in Drosophila display abundant ER-Golgi vesicles and pearled tubes but no megacarriers. *Cell Rep.* 36:109707. https://doi.org/10.1016/j.celrep.2021.109707

Zeuschner, D., W.J.C. Geerts, E. van Donselaar, B.M. Humbel, J.W. Slot, A.J. Koster, and J. Klumperman. 2006. Immuno-electron tomography of ER exit sites reveals the existence of free COPII-coated transport carriers. *Nat. Cell Biol.* 8:377–383. https://doi.org/10.1038/ncb1371

Supplemental material

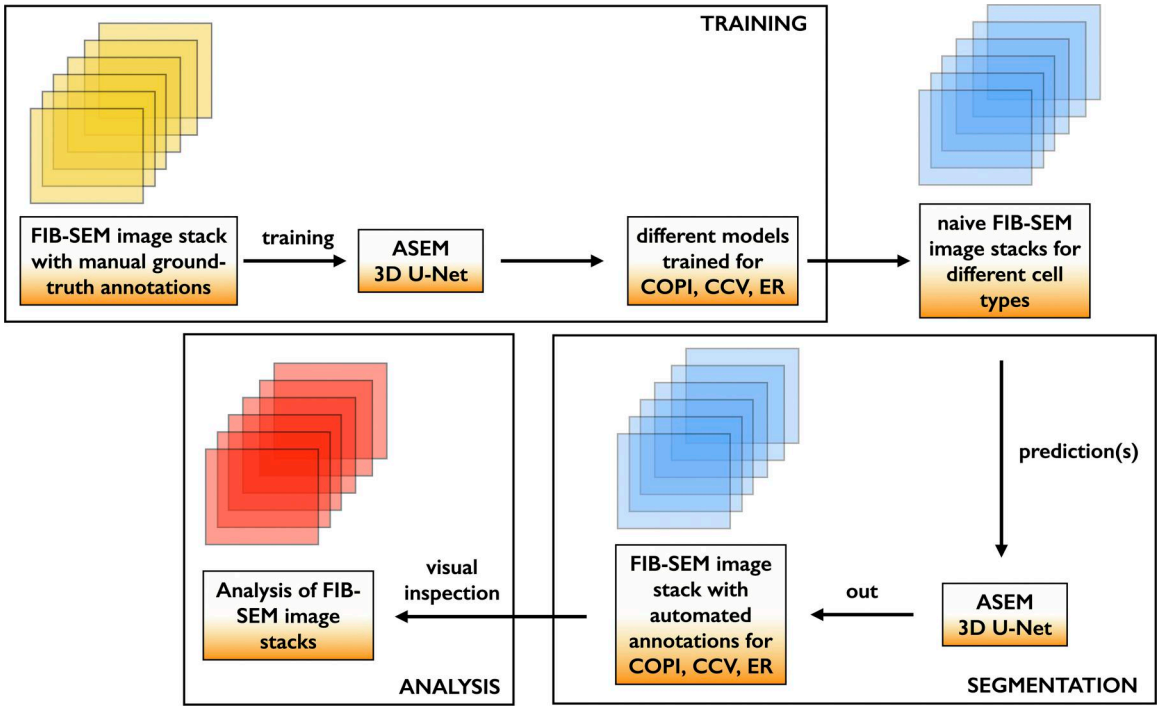

Figure S1. **Workflow for training and application of ASEM models to FIB-SEM datasets.** Manual ground-truth annotations of FIB-SEM image stacks were used to train the ASEM 3D U-Net models. Separate models were generated for COPI-coated vesicles, CCV, and ER. These trained models were then applied to naïve FIB-SEM image stacks from multiple cell types to generate predictive segmentations. Automated annotations were subsequently inspected and validated in the context of the underlying image data, which served as the basis for quantitative and morphological analyses.

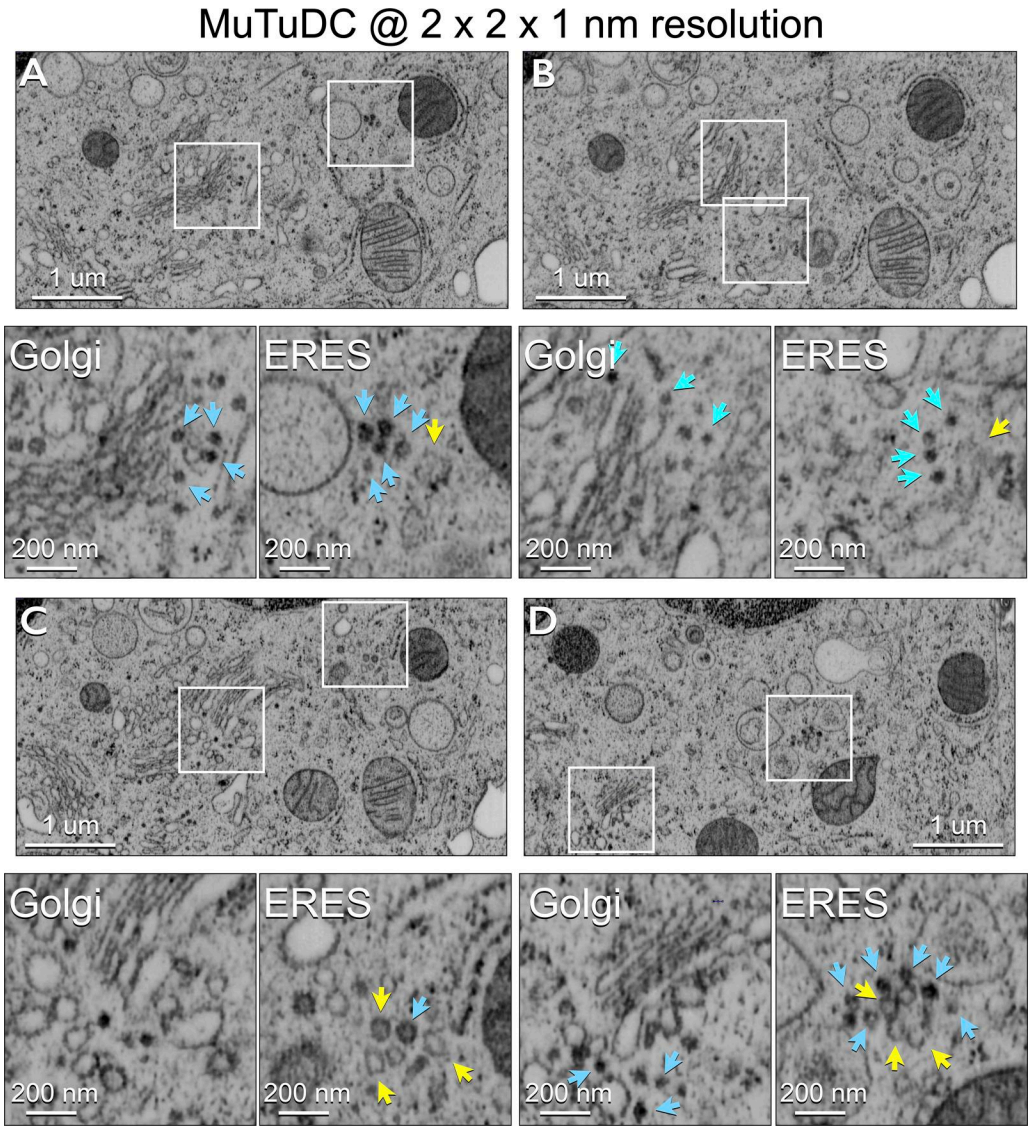

Figure S2. **COPI vesicles near the Golgi apparatus and vesicular ERES (Associated with Video 9).** Single-plane views from a denoised FIB-SEM volume of an interphase MuTuDC cell acquired at 2 × 2 × 1 nm voxel size. Scale bar: 1 µm. Insets (3× enlargement, scale bar: 200 nm) show light blue arrowheads marking visually confirmed isolated COPI vesicles and associated ERES; yellow arrowheads indicate buds emanating from the ER. **(A–D)** correspond to z planes 332, 497, 664, and 1552, respectively.

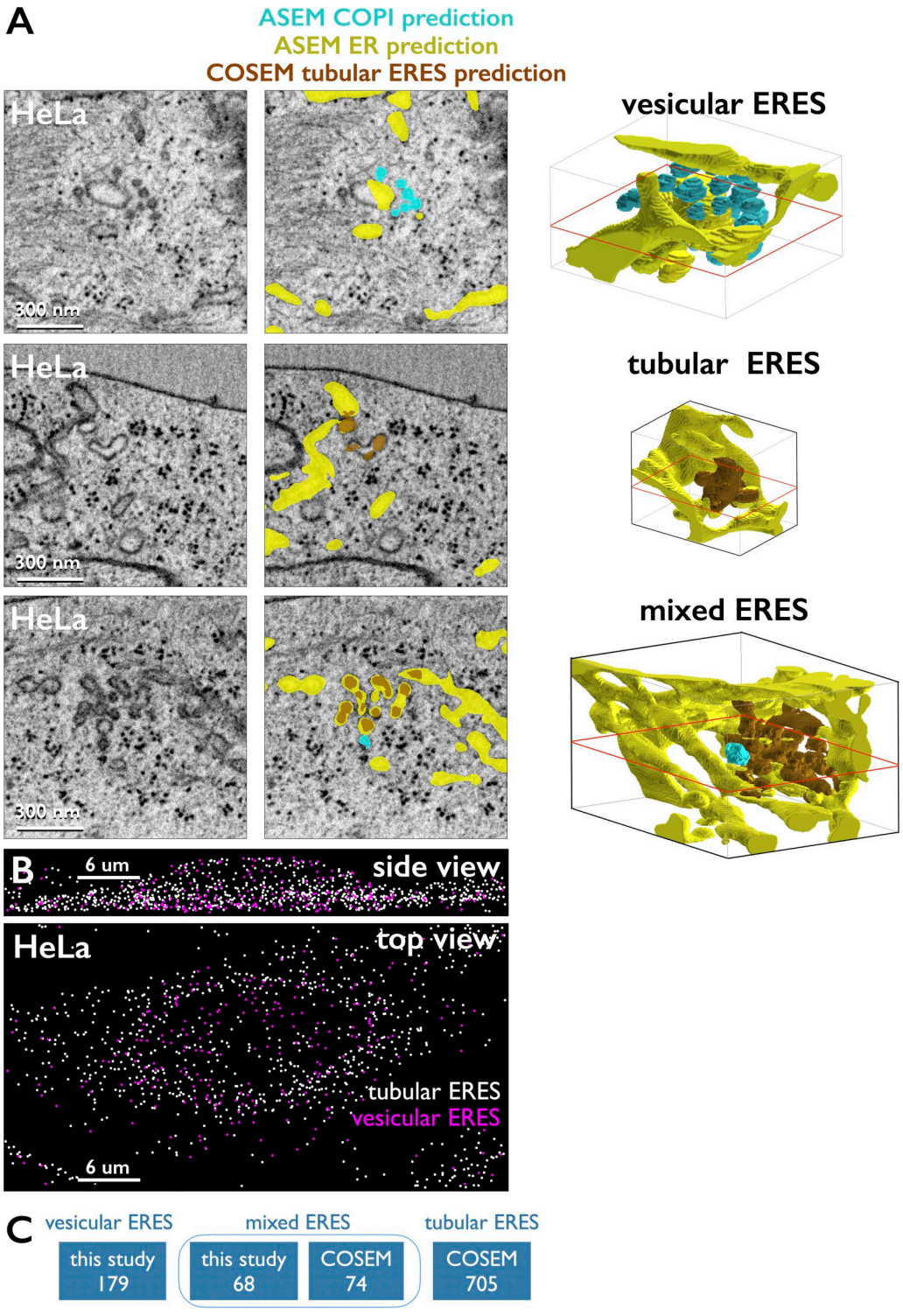

Figure S3. **Comparison of predictions of vesicular and tubular ERES (Associated with** Videos 10, 11, and 12**).** FIB-SEM dataset at 4 × 4 × 5.24 nm voxel size generated by the COSEM is from HeLa-2 cell during interphase prepared by HPFS. **(A)** Left panels: Single-plane views highlight representative examples of stand-alone vesicular and tubular ERES and a case where both types are juxtaposed. Middle panels: Predictions of vesicles (light blue) and adjacent ER (yellow) from ASEM COPI and ER models, and tubular membranes (dark orange) from the COSEM model. Scale bars: 300 nm. Right panels: Manually annotated volumetric renditions of vesicles and ER in single vesicular and tubular ERES and in a region containing both types. **(B)** Top and bottom panels: Z-projection views of centroid positions for vesicular (cyan) and tubular (white) ERES. **(C)** Vesicular ERES (n = 247) were identified using COPI and ER ASEM models; tubular ERES (n = 779) correspond to regions from the same HeLa-2 cell annotated as tubular ERES by the COSEM project using their tubular ERES COSEM model.

Video 1. **Manual annotations of COPI vesicles (blue) adjacent to the Golgi apparatus, rendered through the passing FIB-SEM volume of the same SVG-A cell shown in Fig. 2, A and B, using WEBKNOSSOS.**

Video 2. **Manual annotations of COPI-coated vesicles (blue) and CCVs (cyan) adjacent to the Golgi apparatus, rendered through the FIB-SEM volume of the SVG-A cell shown in Fig. 2 C, using WEBKNOSSOS.**

Video 3. **Manual annotations of COPI vesicles (blue) adjacent to the Golgi apparatus, rendered through the passing FIB-SEM volume of the iN cell shown in Fig. 2 D, using WEBKNOSSOS.**

Video 4. **Manual annotations of COPI vesicles (blue) adjacent to the Golgi apparatus, rendered through the passing FIB-SEM volume of the HeLa cell shown in Fig. 2 E, using WEBKNOSSOS.**

Video 5. **Manual annotations of COPII vesicles (blue) adjacent to the annotated ER (yellow), identified as vesicular ERES rendered through the passing FIB-SEM volume of the SVG-A cell shown in Fig. 3 A, using WEBKNOSSOS.**

Video 6. **Manual annotations of COPII vesicles (blue) adjacent to the annotated ER (yellow), identified as vesicular ERES rendered through the passing FIB-SEM volume of the iN cell shown in Fig. 3 B, using WEBKNOSSOS.**

Video 7. **Manual annotations of COPII vesicles (blue) adjacent to the annotated ER (yellow), identified as vesicular ERES rendered through the passing FIB-SEM volume of the HeLa cell shown in Fig. 3 C, using WEBKNOSSOS.**

Video 8. **Manual annotations of COPI vesicles (blue) adjacent to the Golgi apparatus (green) rendered through the passing FIB-SEM volume of the SVG-A cell shown in Fig. 4.** Annotations were performed using the Labkit plugin in FIJI (Arzt et al., 2022), and masks were exported to Imaris (Bitplane, Zurich, Switzerland) for 3D rendering using the "Surfaces" feature. The movie was generated with the "Animation" tool in Imaris.

Video 9. **Manual annotations of COPII vesicles (blue) adjacent to the annotated ER (yellow), identified as vesicular ERES rendered through the passing FIB-SEM volume of the MuTuDC cell shown in Fig. 5.** Annotations were performed using the Labkit plugin in FIJI (Arzt et al., 2022), and masks were exported to Imaris (Bitplane, Zurich, Switzerland) for 3D rendering using the Surfaces feature. The movie was generated with the Animation tool in Imaris.

Video 10. **Manual annotation of COPII vesicles (blue) adjacent to the annotated ER (yellow), identified as vesicular ERES rendered through the passing FIB-SEM volume of a region of the HeLa cell shown in Fig. S3 A, using WEBKNOSSOS.**

Video 11. **Manual annotation of a tubular ERES (dark orange) adjacent to the annotated ER (yellow), rendered through the passing FIB-SEM volume of a different region of the HeLa cell shown in Fig. S3 A, using WEBKNOSSOS.**

Video 12. **Example of a mixed ERES, illustrated by manual annotations in WEBKNOSSOS.** A single COPII-coated vesicle (blue), adjacent to the annotated ER (yellow), defines a vesicular ERES in close spatial association with a tubular ERES (dark orange). The annotations are rendered through the FIB-SEM volume of a distinct region of the HeLa cell shown in Fig. S3 A.

Provided online is Table S1. Table S1 summarizes the cells and datasets used in this study.